Oxomolybdate anchored on copper for electrocatalytic hydrogen production over the entire pH range

Xiaolong Zhang[a], Ying Zhang[a], Fengwang Li[a], Christopher D. Easton[b], Alan M. Bond[a], Jie Zhang[a],*

[a] *School of Chemistry, Monash University, Clayton 3800, Victoria, Australia*
[b] *CSIRO Manufacturing, Bayview Avenue, Clayton 3168, Victoria, Australia*

ARTICLE INFO

ABSTRACT

Uniting the advantages of molecular and heterogeneous catalysts, a continuing effort in heterogeneous catalysis, has often proved to be challenging. This work introduces a facile strategy to obtain molybdenum-oxo functional groups strongly anchored on metallic copper support through *in situ* electrochemical reduction of a cuprous oxomolybdate thin film resulting from electroless plating. The oxomolybdate modified copper electrode exhibits enzyme-like activity and excellent stability for the hydrogen evolution reaction over the entire pH range, together with excellent mechanical properties and cost effectiveness that are needed for commercial applications, including seawater electrolysis. *In situ* Fourier transformed ac voltammetric study revealed two underlying $Mo^{IV/III}$ and $Mo^{III/II}$ processes that are responsible for the high catalytic activity of the material. This study opens up a new avenue for designing advanced heterogeneous catalysts for a greener future using a broad range of oxometalates.

1. Introduction

Homogeneous molecular catalysts can be rationally designed and optimized at the atomic level. They often show high catalytic activity per molecule and high selectivity under benign conditions, but the stability, separation and reutilization may be problematic. While heterogeneous catalysts have the advantages of recyclability, i.e. ease of separation from the reaction mixture, high stability, and can be used in continuous flow processes, they often have limited active site density. [1] One of the continuing efforts in catalysis is to unite the advantages of homogeneous and heterogeneous catalysts for green and sustainable chemistry by immobilizing a molecular catalyst onto a high surface area solid support. To fabricate this kind of catalyst, a molecular catalyst is first synthesized, often through a tedious procedure, with additional structural moieties introduced to stabilize the catalytically active site. However, this procedure unavoidably diminishes the density of active sites when the molecular catalyst is immobilized on the solid support. Furthermore, a linker is often required to covalently immobilize the molecular catalyst on the solid support, [2–4] which hinders effective electronic communication between the catalyst and the support [5]. Ideally, to maximize the density of active sites on the support and to maintain their activity, use of linker or other structural moieties should be avoided.

Electrocatalytic hydrogen production by electrolysis of seawater using renewable energy represents a highly attractive goal of catalysis. [6–12] Identifying efficient electrocatalysts based on earth abundant elements for the hydrogen evolution reaction (HER) in both neutral and alkaline media (see later discussion) is one of the key challenges to realize this goal [13–21]. The development of molecular HER catalysts that functionally mimic the water reduction chemistry of hydrogenases have inspired the discovery of some highly efficient aqueous compatible molecular HER catalysts [22–27]. Oxo-metallates reported by Long and co-workers [28], which catalyze the HER in a neutral phosphate buffer (PB) solution to generate hydrogen under ambient conditions, are among the most attractive ones, although their performance has not met the requirement for commercial applications. Inspired by their study, in this paper, we demonstrate a facile strategy for strongly anchoring molybdenum-oxo HER active sites on metallic copper substrates using a readily available precursor to achieve Pt-like HER activity in both neutral and alkaline media, along with unprecedentedly high HER activity for this class of materials in acidic media.

---

* Corresponding author.
  E-mail address: jie.zhang@monash.edu (J. Zhang).

2. Experimental section

2.1. Materials and instrumentation

Copper plate (99.99%) was purchased from ZNXC (China), $Na_2MoO_4·2H_2O$ (99.0%), $CuSO_4·5H_2O$ (99.0%) and 5% Nafion solution from Sigma-Aldrich, NaH_2PO_4 (99.0%), Na_2HPO_4 (99.0%), KOH (99.0%), H_2SO_4 (98%), and formamide (99.0%) from Merck. All chemicals were used as supplied by the manufacturer. Aqueous solutions were prepared using high purity water obtained from a Milli Q water (18.2 MΩ cm) purification system.

Transmission electron microscopy (TEM) images were collected with a FEI Tecnai G2 T20 TWIN TEM instrument. Aberration-corrected high-angle annular dark-field scanning transmission electron microscopy (HAADF-STEM) images and energy-dispersive X-ray spectra (EDS) were acquired with a FEI Tecnai G2 F20 S-TWIN FEGTEM instrument operated at 200 kV. Gas chromatography (GC) was performed with an Agilent 7820 A gas chromatography system equipped with a HP–plot molesieve (5 Å) column and a thermal conductivity detector (TCD). The carrier gas was nitrogen (99.99%) for H_2 analysis. The retention time was compared with that obtained with an authentic sample of H_2 gas.

2.2. Methods

2.2.1. Electrodeposition of copper foam

Copper foam was prepared by a hydrogen bubble templated electrodeposition method adopted from the literature.[1] Copper plate was used as the substrate for the electrodeposition. A Hg/Hg_2SO_4 (saturated K_2SO_4) was used as reference electrode and a graphite rod was used as the counter electrode. The electrolyte solution contained 0.4 M $CuSO_4$ and 1.2 M H_2SO_4. A constant potential of -4.4 V was applied for 6 s to electrodeposit porous copper dendrite onto the copper substrate. The as prepared copper foam was then rinsed thoroughly with high purity water and acetone and then dried in air.

2.2.2. Synthesis of $Cu_4Mo_5O_{17}$ thin films on a copper substrate

Commercial copper plates were polished with emery paper and rinsed with ethanol before use. A piece of polished copper plate or freshly prepared copper foam was immersed into a mixed solution of formamide and 0.2 M Na_2MoO_4 aqueous solution in a beaker which was stored in a fume hood for 24 h. During this time, the color of the copper substrate changed from reddish-orange to dark brown. Finally, the copper plate/foam was removed from the beaker and rinsed thoroughly with water and acetone and dried in air.

2.2.3. Synthesis of $CuMoO_4$ powder and preparation of $CuMoO_4$ modified glassy carbon electrodes

$CuMoO_4$ powder was prepared by a precipitation reaction between $CuSO_4$ and Na_2MoO_4. In detail, 5 mL 0.1 M $CuSO_4$ aqueous solution was first mixed with 5 mL 0.1 M Na_2MoO_4 aqueous solution. After stirring for 10 min, the green precipitate formed was collected by centrifugation and washed with water and ethanol. Next, the green precipitate was dried in an oven at 80 °C to obtain $CuMoO_4$. To prepare a $CuMoO_4$ modified glassy carbon electrode, 2.0 mg of $CuMoO_4$ was dispersed in a mixed solution containing 600 μL ethanol, 300 μL water, and 20 μL 5% Nafion solution. After ultrasonication for 10 min, 6 μL of the mixed solution was drop-casted onto a glassy carbon electrodes.

2.2.4. Electrochemical instrumentation and procedures

All electrochemical experiments were performed at room temperature (22 °C) unless otherwise stated using a standard three-electrode cell configuration with a CHI700D electrochemical workstation (CHI Instruments, Austin, Texas, USA). Materials described above were used as the working electrodes (cathode) with graphite rod as the counter electrode (anode). Reference electrodes were chosen on the basis of the pH of the electrolyte solution: Hg/Hg_2SO_4 (saturated K_2SO_4) for acidic solutions, Ag/AgCl (3 M KCl) for neutral solutions, and Hg/HgO (1 M NaOH) for alkaline solutions. The scan rate used in all linear sweep voltammetric (LSV) experiments was 10 mV s^{-1}. Potentials while measured vs the reference electrode are converted to the reversible hydrogen electrode (RHE) scale using the formula: E(vs. RHE) = E(vs. ref.) + $E°_{ref}$ + 0.0586 × pH. Bulk electrolysis was conducted in a gas tight two-compartment H-shaped electrolysis cell under a N_2 atmosphere, with a porous glass frit separating the anodic and cathodic half-cells. High purity N_2 gas was introduced to remove oxygen prior to electrochemical measurements. After N_2 bubbling for approximately 20 min, the electrolysis cell was sealed tightly with a rubber stopper. The controlled potentials used during bulk electrolysis were selected on the basis of voltammetric data obtained under relevant conditions. Fourier Transformed alternating current voltammetric (FTacV) experiments were carried out using a home-built instrument [2] with an applied sine wave perturbation having an amplitude (ΔE) of 80 mV and a frequency (*f*) of 9.00 Hz.

2.2.5. Analysis of the electrolysis products

Gas chromatography was used to identify gaseous products in the headspace. Calibration curves for H_2 were constructed by injecting a known amount of pure H_2 and plotting the peak area against the amount injected. The gaseous product was identified by comparing the retention time with pure standard H_2 gas and quantified from the relevant calibration curve.

2.2.6. XPS characterization

X-ray photoelectron spectroscopy (XPS) analysis was performed using an AXIS Ultra DLD spectrometer (Kratos Analytical Inc., Manchester, UK) with a monochromatic Al K_α source at a power of 180 W (15 kV × 12 mA) or 168 W (14 kV x 12 mA), a hemispherical analyser operating in the fixed analyser transmission mode and the standard aperture (analysis area: 0.3 mm × 0.7 mm) The total pressure in the main vacuum chamber during analysis was typically in the range of 10^{-9} to 10^{-8} mbar. Survey spectra were acquired at a pass energy of 160 eV. To obtain more detailed information on the chemical structure and oxidation states etc., high resolution spectra were recorded from individual peaks using a 40 eV pass energy (yielding a typical peak width for polymers of < 0.9 eV).

Each specimen was analysed by XPS at an emission angle of 0° as measured normal to the surface. Assuming typical values for the electron attenuation length of relevant photoelectrons, the XPS analysis depth (from which 95% of the detected signal originates) ranges between 5 and 10 nm for a flat surface. Since the actual emission angle is ill-defined in the case of particles and powders (ranging from 0° to 90°), the sampling depth in these cases may range from 0 to approx. 10 nm.

XPS data processing was performed using CasaXPS software version 2.3.15 (Casa Software Ltd., Teignmouth, UK). All elements present were identified from survey spectra. The atomic concentrations of the detected elements were calculated using integral peak intensities and the sensitivity factors supplied by the manufacturer. Binding energies were referenced to the C 1 s peak at 284.8 eV (aliphatic hydrocarbon). The accuracy associated with quantitative XPS is ca. 10%–15%. Precision (i.e. reproducibility) depends on the signal to noise ratio but is usually significantly better than 5%. The latter result is relevant when comparing similar samples.

3. Results and discussion

The electrode developed in this study was prepared by a one-step chemical method, as illustrated in Fig. 1a. When a freshly polished copper electrode was placed in an aqueous solution containing formamide and Na_2MoO_4 under ambient conditions, a dark brown thin film gradually formed in 24 h. Optimization of synthesis conditions for growing the thin film is discussed in detail in SI (Figures S1 to S5 and
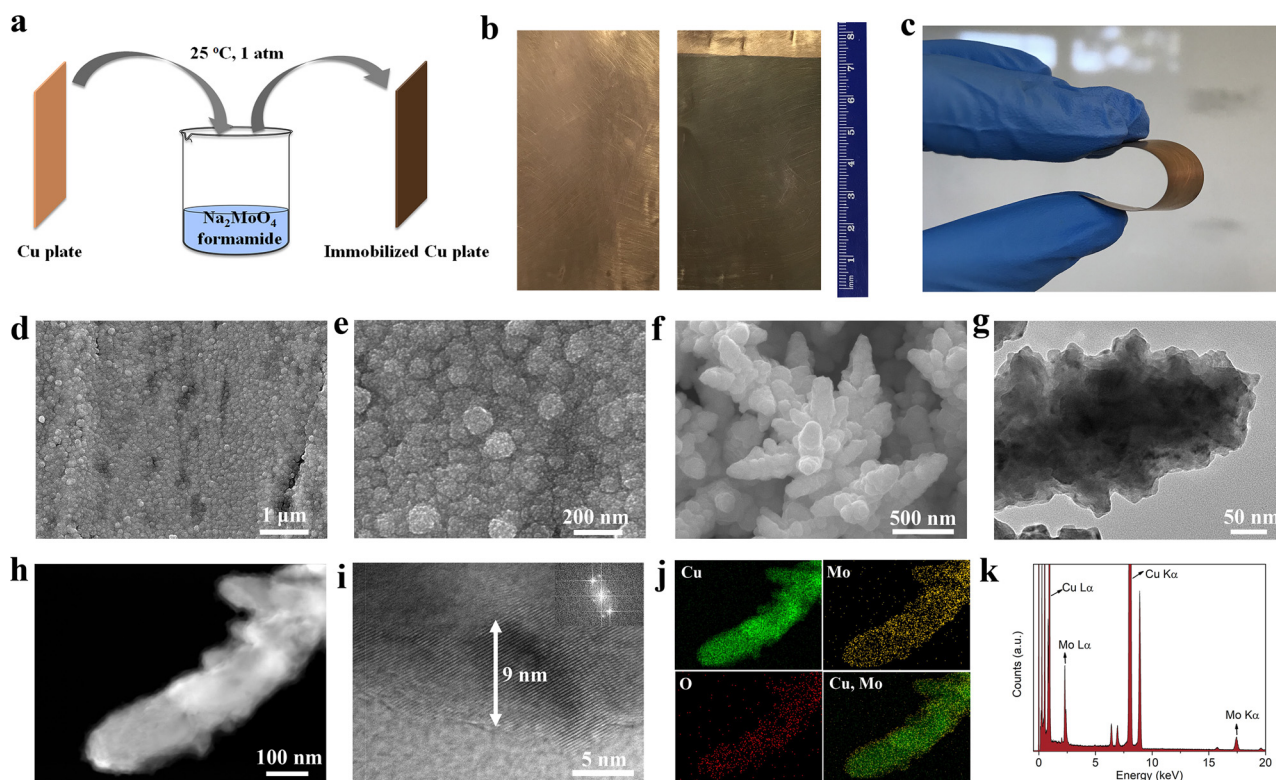
Fig. 1. (a) Schematic illustration of the synthesis process. (b) Photograph of copper plate with (right) and without (left) a surface film. (c) Photograph showing the flexibility of the immobilized copper plate. (d,e) SEM images of the thin film grown on copper plate. (f) SEM images of the thin film grown on electrochemical deposited copper dendrites. (g) TEM image of the thin film grown on a copper dendrite. (h) STEM-HAADF image of a copper dentrite with the thin film. (i) HRTEM image of the film on the surface of a copper dendrite. Inset is the corresponding FFT transformed image. (j) EDX mapping images of a copper dendrite with the thin film. (k) An EDX spectrum.

the relevant text). The thin compact film can grow on any kind of copper substrate, such as copper plate, copper foil, and copper foam. Fig. 1b shows a photograph of two pieces of copper plate with (right) and without (left) the film. The modified copper plate can be bent 180° (Fig. 1c), yet the film can remain tightly adhered to the substrate. This film cannot be peeled off with scotch tape (not shown). These results demonstrate the mechanical stability and physical flexibility of the film. An SEM image (Fig. 1d) revealed that the film has a rough nanoparticulate surface morphology. In the higher magnification SEM image (Fig. 1e), densely arranged nanoparticles with a size well below 10 nm can be distinguished.

The X-ray diffraction technique was insufficiently sensitive to obtain structural information due to the extreme thinness of the film. Therefore, to reveal structural details of the thin film, high resolution TEM was used. For the convenience of TEM characterization, electrochemically deposited copper dendrites with diameters less than a hundred nanometers were used to grow the film. No clearly defined surface feature of the copper dendrite could be identified under SEM (Fig. 1f). However, high resolution TEM images reveal that the smooth surface of the pristine copper dendrite (Figure S6a) has been transformed into an irregular surface (Figs. S6b and 1g). A surface layer with slightly lower image contrast than the bulk copper was observed in a scanning TEM (STEM) image (Fig. 1h). A high resolution TEM (HRTEM) image (Fig. 1i) reveals a well crystalized surface layer with a thickness of around 9 nm. Three type of lattices were found on the surface of the copper dendrite according to the FFT image (Fig. 1i inset), with d-spacing of 5.20, 2.48, and 2.11 Å. EDX mapping images (Fig. 1j) show that Cu, Mo, and O elements are uniformly distributed on the surface of the copper dendrite. A small peak located at 2.29 keV in the EDX spectrum (Fig. 1k) is assigned to Mo Lα, which further confirms the existence of Mo on the copper dendrite.

A Raman spectrum collected on the film is shown in Fig. 2a. The

Raman band at 902.8 cm^{-1} is attributed to terminal Mo-O vibration, while the band at 531.1 cm^{-1} is the in plane mode of a Mo-O unit. The Cu-O overtone modes are observed at 217.6 and 423.3 cm^{-1}, while the band at 642.8 cm^{-1} is assigned to the forbidden mode of Cu-O units [29,30]. To provide additional evidence on the composition of the surface layer, the sample was characterized by XPS. Fig. 2b shows the Mo 3d peaks, which are assigned to Mo(VI) based on the position and shape, in accordance with the literature [31]. Fig. 2c shows the high-resolution Cu 2p spectrum, while Fig. 2d shows the high-resolution spectrum of the Cu Auger region (Cu L$_3$M$_{4,5}$M$_{4,5}$). No peak associated with Cu(0) was observed in the Auger spectra. The overall peakshapes for the Cu 2p and LMM spectra are indicative of Cu(I). The assignment for Cu(I) was confirmed from the calculated Auger parameter and comparing with the literature value [32]. Materials that simultaneously contain Cu(I) and Mo(VI) are most likely to be cuprous oxomolybdate. Furthermore, the lattices with d-spacing of 5.20, 2.48, and 2.11 Å observed in the HRTEM image before, match with the (120), (1,-1,2), and (-3,-1,3) lattices of Cu$_4$Mo$_5$O$_{17}$ (JCPDS no. 81-1106), respectively. On the basis of the above results, the composition of the thin film is concluded to be Cu$_4$Mo$_5$O$_{17}$. The reaction that leads to the formation of the Cu$_4$Mo$_5$O$_{17}$ (CMO) film is proposed below:

$$4Cu + 5MoO_4^{2-} + O_2 + 5H_2O \xrightarrow{formamide} Cu_4Mo_5O_{17} \downarrow + 10OH^- \tag{1}$$
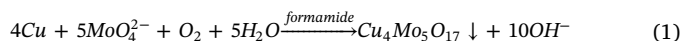
Although formamide is not directly involved in this reaction, it speeds up the formation of the CMO film. It is well known that the oxidation of metallic Cu can be facilitated by the presence of electronegative ligands. For example, the standard reduction potential for the Cu/Cu$^+$ process changes from 0.518 V to -0.119 V in the presence of ethylenediamine. Analogously, the presence of formamide in the reaction medium can facilitate the formation of Cu$^+$, and consequently the CMO film. CMO was previously synthesized under high temperature
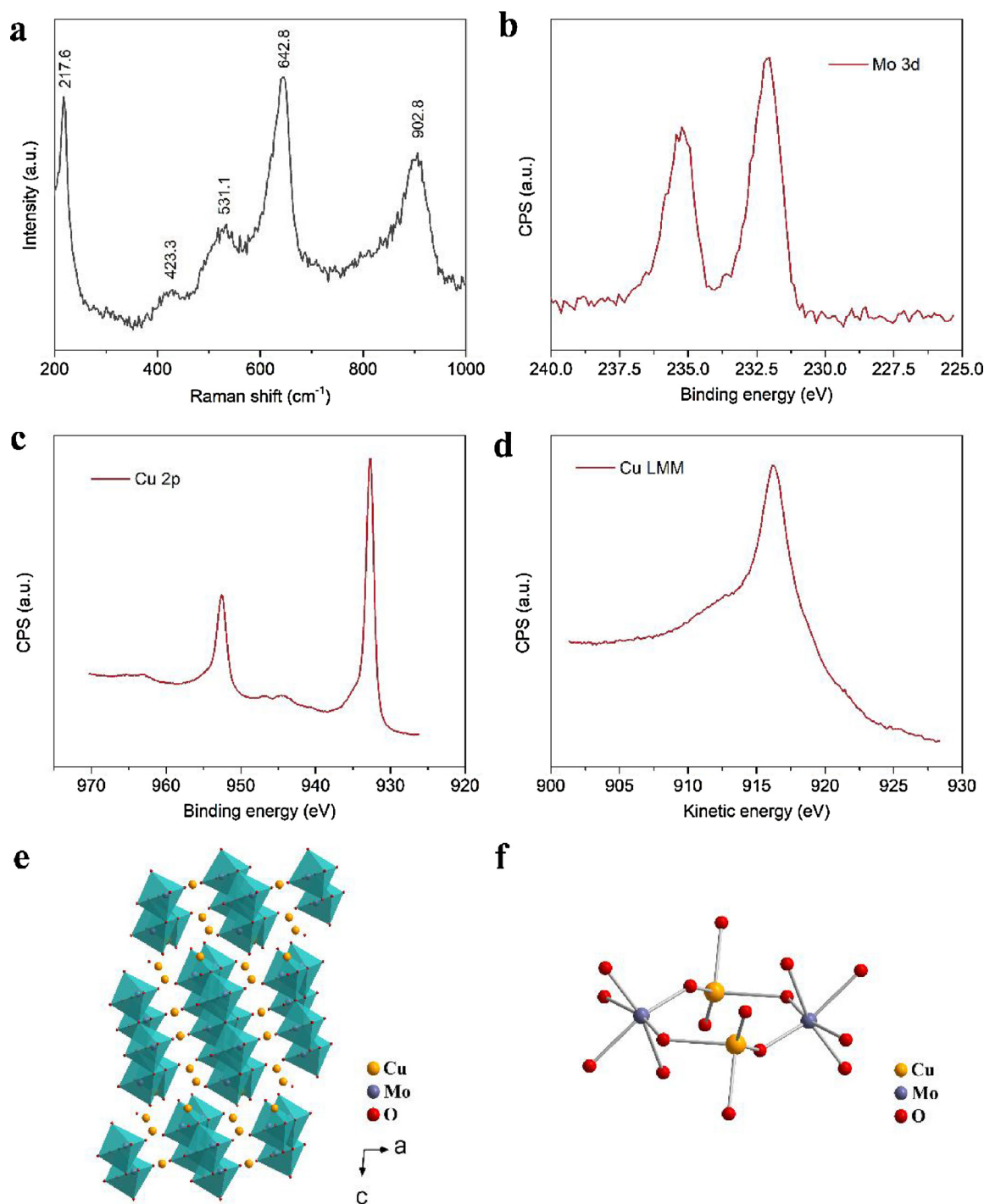
Fig. 2. (a) Raman spectrum of the CMO film (488 nm excitation source). (b–d) XPS spectra of: b) Mo 3d, c) Cu 2p, d) Cu LMM obtained from the surface of the CMO film. (e) Structure view of CMO along the b axis. (f) Three-dimensional illustration of the Cu-Mo-O motif with an O bridging structure.

conditions. [33–35] This is the first observation of the formation of CMO under ambient conditions. The structure of the CMO film is shown in Fig. 2e and consists of chains of edge-sharing MoO_6 octahedra and sheets of corner sharing CuO_4 tetrahedra based on the literature [34]. CMO constitutes a three-dimensional structure (Fig. 2f) where bridging O connect both Cu and Mo centers.

To investigate the catalytic performance towards the hydrogen evolution reaction, planar Cu plates modified with CMO (Cu plate@CMO) were used as working electrodes. The geometric current density obtained from the Cu plate@CMO electrode in 0.5 M PB (pH 7), 1 M KOH (pH 14) and 0.5 M H_2SO_4 (pH 0.33) solutions was compared

with that of a Pt wire to assess the feasibility for commercial applications (Fig. 3). The Cu plate@CMO exhibits much enhanced HER activity in comparison with a bare Cu plate at all pH values. The HER activity of the Cu plate@CMO electrode is close to that found at the Pt wire electrode in the 0.5 M PB solution (Fig. 3a). Thus, an overpotential of 270 mV is required to reach a current density of 10 mA cm^{-2}, compared with 171 mV for the Pt wire electrode. The onset potential (arbitrarily defined as the potential needed to reach 1 mA cm^{-2}) of the Cu plate@CMO is only 71 mV. In a 1 M KOH solution (Fig. 3b), the Cu plate@CMO electrode requires 252 mV of overpotential to reach 10 mA cm^{-2}, 100 mV higher than that of Pt wire. In acidic medium (Fig. 3c),
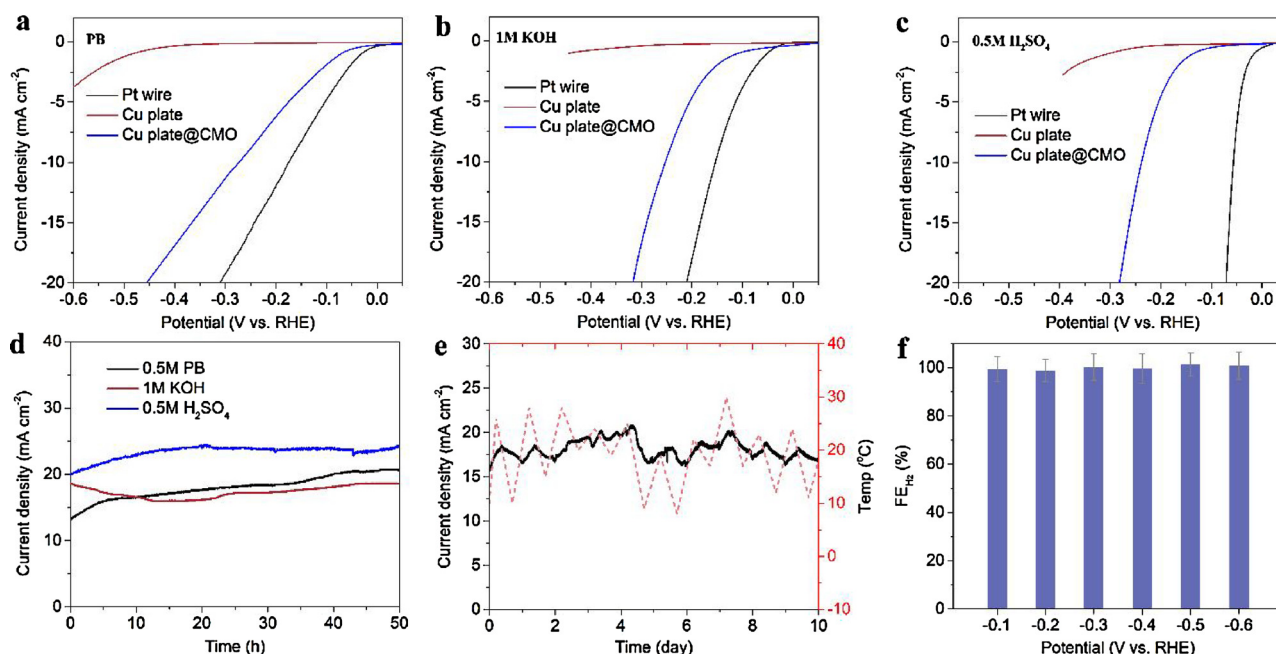
Fig. 3. (a–c) Polarization curves for Pt wire, Cu plate, and Cu plate@CMO in a) 0.5 M phosphate buffer, b) 1 M KOH solution, and c) 0.5 M H_2SO_4 solution. (d) Current density-time curves collected at 300 mV overpotential on a Cu plate@CMO electrode in 0.5 M pH 7 PB, 1 M KOH, and 0.5 M H_2SO_4. (e) Current density-time curve for a 10 days stability test at 300 mV overpotential on a Cu plate@CMO electrode in 0.5 M pH 7 phosphate buffer plotted together with temperature variation during the test period. (f) Hydrogen faradaic efficiency as a function of applied potential collected on a Cu plate@CMO electrode in pH 7 phosphate buffer. All current densities are calculated based on the geometric surface area.

the performance of Cu plate@CMO is not comparable to the Pt wire but outperforms other state-of-art catalysts in the same category. [15,36] $CuMoO_4$ prepared by a precipitation reaction between Cu^{2+} and MoO_4^{2-} was also prepared and tested as a HER catalyst in 0.5 M PB solution (Figure S7). Compared to $CuMoO_4$, the HER activity of Cu plate@CMO is significantly enhanced, which is attributed to the thinness of the CMO film, which facilitates excellent electronic communication between molybdenum-oxo active sites and the conductive Cu support. By contrast, the Cu content in $CuMO_4$ is insufficient to produce a continuous conductive Cu metal support under HER conditions.

In order to investigate the stability of the CMO catalyst, the Cu plate@CMO electrode was subjected to long-term bulk electrolysis at 300 mV overpotential in 0.5 M H_2SO_4, 0.5 M PB (pH 7) and 1 M KOH solutions. Fig. 3d shows the current density-time curves. The CMO catalyst showed excellent stability for at least 50 h in all solutions, with steady state catalytic current densities achieved of around 23, 18, and 17 mA cm^{-2}, respectively. Fig. 3e shows a longer 10-day stability test of the Cu plate@CMO catalyst in the phosphate buffer solution under environmentally relevant conditions. Again, the catalyst exhibited excellent stability. Current variation is attributed to temperature fluctuation during this period since there is an excellent correlation between these two parameters as shown in Fig. 3e. Cross-section SEM images of the Cu plate@CMO electrode before and after the long-term stability test (Figure S8) show that the surface film has remained tightly adhered to the copper substrate. Noteworthily, the Cu plate@CMO demonstrated much enhanced HER activity and high stability at 70 °C, the operational temperature for a commercial water electrolyser, as shown in Figure S9. Stable catalytic current densities of about 150, 220, and 195 mA cm^{-2} at 270 mV overpotential were achieved in 0.5 M PB, 1 M KOH, and 0.5 M H_2SO_4 solutions, respectively. The high stability of the Cu plate@CMO is attributed to the strong adhesion of the CMO layer as well as the stability of the copper substrate under HER conditions over the whole pH range and in accordance with the copper Pourbaix diagram. [37] The mechanically flexible and robust characteristics of the Cu plate@CMO ensure wide application for HER under harsh circumstances [38]. In addition to establishing the stability, it is

also very important to determine the faradaic efficiency of the catalytic process. An air-tight H-type electrolysis cell separated by a glass frit was used for bulk electrolysis utilizing the Cu foam@CMO catalyst. The H_2 gas product was detected by GC and quantified using a standard calibration curve. Fig. 3f shows the faradaic efficiency for H_2 (FE_{H2}) determined at applied potentials ranging from -0.1 to -0.6 V. At all potentials applied, FE_{H2} values are close to 100%, and no other products were detected. Since the activity of the electrode depends on the density of active sites, in principle, by changing to a three-dimensional electrode structure using a highly porous electrode, the electrode performance should be greatly enhanced. [16,39–41] Indeed, even when the CMO film is grown on an electrodeposited copper foam (Figure S10) under non-optimized conditions, it exhibited a level of performance that surpasses Pt wire in neutral medium and provided similar performance with Pt wire in alkaline medium on the basis of current per geometric area (Figure S11). The large catalytic current density for Cu foam@CMO is attributed to its high electrochemically-active surface area (ECSA), as indicated by electrochemical double layer capacitance tests (Figure S12). It is worth noting that the Cu foam@CMO performance in neutral conditions equals that of the most active HER catalysts in this medium, as shown in Table S4. In 0.5 M H_2SO_4 solution, the performance of the porous electrode is also greatly improved, as expected, although an additional 136 mV overpotential is required to reach 10 mA cm^{-2} in comparison with the Pt wire electrode.

The fact that CMO exhibits Pt-like HER activity and excellent long-term stability in both neutral and alkaline media in addition to having advantages highlighted earlier makes it an excellent candidate for seawater electrolysis. [42] During seawater electrolysis, the cathodic reaction is the HER. The major anodic reaction is the formation of chlorine, an industrial chemical, since Cl^- conversion to Cl_2 is kinetically more favourable than the oxygen evolution reaction. The overall reaction is described in the following equation,

$$2H_2O + 2Cl^- \rightleftharpoons H_2 + 2OH^- + Cl_2 \qquad (2)$$
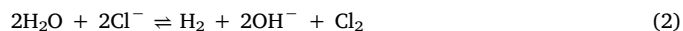
Therefore, during electrolysis, an initially neutral solution will turn into an alkaline one. Thus, seawater electrolysis requires the HER

catalyst to be stable and active in both neutral and alkaline conditions, which is exactly the case for the CMO.

Even though PB (pH 7) and seawater are both neutral media, they are different with respect to the HER in terms of the source of proton. In phosphate buffer, the direct source of proton is $H_2PO_4^-$ which is the strongest acid in this medium (pK_a = 7.2), as demonstrated in Figure S13. In seawater, where NaCl is the dominant electrolyte, the source of proton for the HER is the water molecule (pK_a = 14) which has much higher basicity than $H_2PO_4^-$. There has been some technical challenges associate with seawater electrolysis, such as precipitation of Mg(OH)$_2$. [42,43] In the proof of concept study, chlor-alkali water was used as a simplified version of seawater to confirm the activity and stability of CMO in this medium. The HER activity of the Cu plate@CMO electrode was tested in aqueous 0.5 M NaCl and found to be comparable to Pt (Figure S14). A video demonstrating seawater (taken from Port Phillip Bay, Melbourne, Australia) electrolysis driven by a solar panel with Cu plate@CMO as the cathode and nickel foam as the anode is shown in Movie S1.

To provide insights into the mechanistic details of the CMO catalysed HER, FTacV was employed. In FTacV, a large amplitude periodical ac waveform is superimposed onto the direct current (dc) ramp. This technology generates higher order ac harmonic components that are devoid of background charging current and insensitive to catalytic process. [44–47] These features allow two fast underlying electron

transfer processes to be detected in the 6th harmonic ac component in all three electrolyte media (Figs. 4 and S15) in the potential region where the HER is initiated. To assign the origin of the two electron transfer processes, the oxidation state of Mo on the electrode after electrolysis at -0.6 V for 0.5 h was first determined by *ex situ* XPS (Figure S16 to S21). Mo^{VI} (over 90%) and Mo^{IV} (1–5%) are present in all samples (Table S1 and S2). The presence of molybdenum suboxide or Mo(0) is also detected in acidic and alkaline conditions. A mixed valance state for Mo is highly desirable since it enhances the conductivity of the CMO under catalytic turnover conditions. [35] Amorphous regions on CMO coated Cu dendrite post bulk electrolysis observed under TEM (Figure S22) are attributed to MoO$_x$. The electrodes were further treated at 0.1 V for half an hour and XPS spectra were taken to obtain the valance state of Mo under non-catalytic turnover conditions. No obvious change in XPS spectra was detected. This is unsurprising due to the rapid turnover of Mo active sites under the HER conditions. Thus, Mo active sites remained at the resting state after the electrodes were prepared under both applied potential conditions. Based on the results obtained by Long and co-workers, [28,48] the catalytically active sites most probably contain Mo^{IV} that undergoes two one-electron transfer steps to generate Mo^{II} that is active for the HER. On this basis, the two underlying electron transfer processes observed under FTacV conditions are assigned to sequential Mo$^{IV/III}$ and Mo$^{III/II}$ reactions. The HER mechanism on the CMO film proposed and
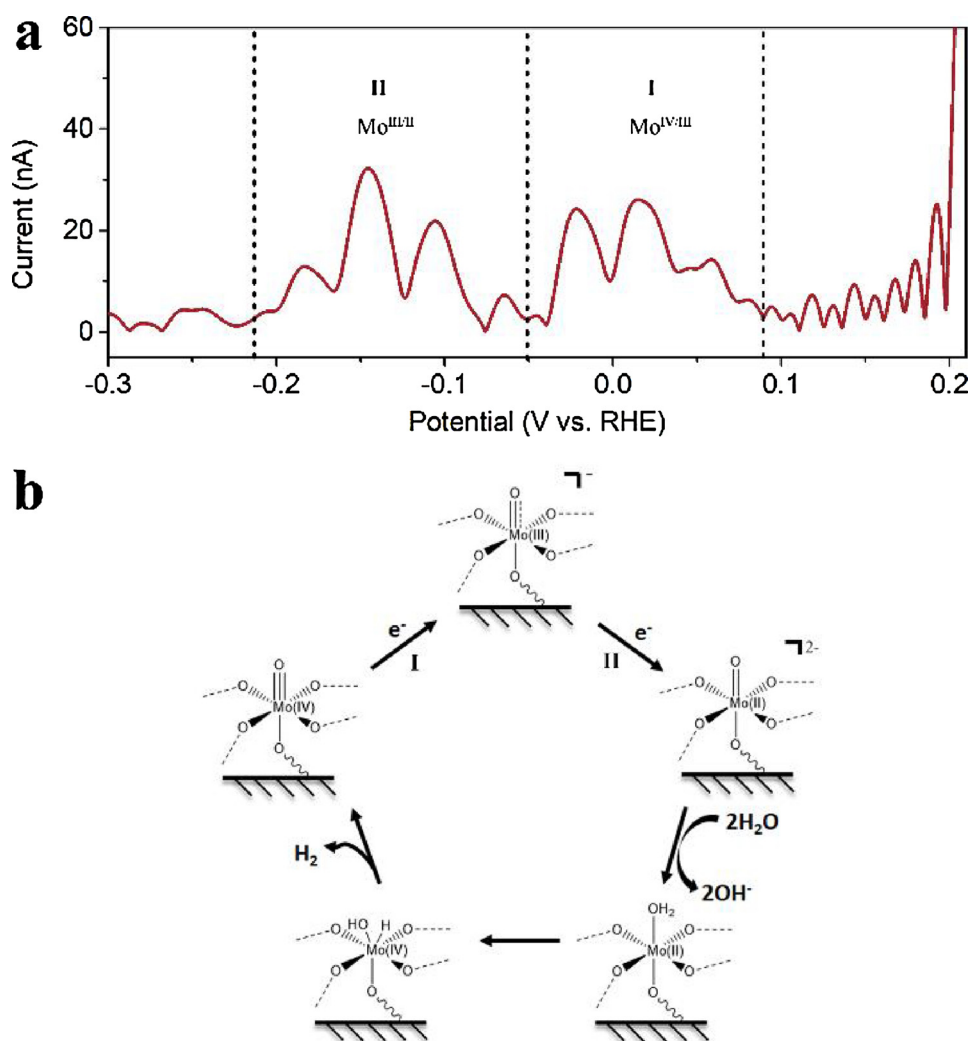
Fig. 4. (a) 6th harmonic components of FTac voltammogram obtained from a CMO immobilized copper electrode in degassed 1 M KOH solution. Parameters: frequency = 9.00 Hz, amplitude = 80 mV, and scan rate = 24.21 mV s^{-1}. (b) Schematic representation of the HER mechanism with a CMO immobilized copper electrode.

illustrated in Fig. 4b is analogous to that proposed by Long and co-workers. The fact that well-defined 6th (Figs. 4a and S15) and higher (not shown) harmonic components were obtained suggests that the $Mo^{IV/III}$ and $Mo^{III/II}$ processes are fast (reversible or very close to reversible). On this basis, comparison of experimental data with simulated ones for a reversible surface confined one-electron transfer process allows the surface coverage of the molybdenum-oxo functional groups to be estimated. The fundamental principles associated with the advanced dynamic FTacV electrochemical technique have been summarised in recent review articles. [49–51] The results in Figure S23 show that good agreement between the experiment and theory is obtained with a surface coverage of 4×10^{-10} mol cm^{-2}. With this information, Eq. (3) was then used to calculate the turnover frequency (*TOF*) value:

$$TOF = i/nNF \quad (3)$$

where i is current, n is the number of electrons transferred to obtained one product molecule, N is the number of catalytically active sites in moles and F is the Faraday constant. Accordingly, turnover frequencies at 300 mV overpotential are calculated to be 257, 185, and 175 s^{-1} per active site in 0.5 M H_2SO_4, 0.5 M PB, and 1 M KOH solutions, respectively, which are significantly larger than that of the published molecular molybdenum-oxo catalyst [28] and comparable to that of hydrogenase enzymes [52].

4. Conclusions and perspectives

In conclusion, a facile method has been developed to grow a thin film of CMO under ambient conditions. *in situ* electrochemical reduction of the CMO film leads to the formation of molybdenum-oxo functional groups strongly anchored on a metallic copper substrate, which exhibits high activity and stability for the HER over the entire pH range. XPS and an *in situ* FTacV study revealed two underlying electron transfer processes which are assigned to $Mo^{IV/III}$ and $Mo^{III/II}$ reactions at the initial stage of HER that are responsible for the high catalytic activity of the material. The MoO_6 functional groups not only mimic the essential configuration of a molecular oxomolybdate HER catalyst, but also anchor tightly with the copper substrate, enabling favorable orientation of the active sites and fast interfacial electron transfer. When a large surface area Cu foam was used as the support, the resultant electrode showed platinum-like activity in both neutral and alkaline media, making it an excellent electrocatalyst for seawater electrolysis.

Acknowledgements

Appendix A. Supplementary data

Supplementary material related to this article can be found, in the online version, at doi:https://doi.org/10.1016/j.apcatb.2019.02.058.

References

[1] S. Sankaranarayanapillai, S. Volker, W.R. Thiel, Magnetically separable nanocatalysts: bridges between homogeneous and heterogeneous catalysis, Angew. Chem. Int. Ed. 49 (2010) 3428–3459.

[2] T. Fukushima, W. Drisdell, J. Yano, Y. Surendranath, Graphite-conjugated Pyrazines as molecularly tunable heterogeneous electrocatalysts, J. Am. Chem. Soc. 137 (2015) 10926–10929.

[3] R.L. McCreery, Advanced carbon electrode materials for molecular electrochemistry, Chem. Rev. 108 (2008) 2646–2687.

[4] J. Pinson, F. Podvorica, Attachment of organic layers to conductive or semiconductive surfaces by reduction of diazonium salts, Chem. Soc. Rev. 34 (2005) 429–439.

[5] J. Wang, X. Ge, Z. Liu, L. Thia, Y. Yan, W. Xiao, X. Wang, Heterogeneous electrocatalyst with molecular cobalt ions serving as the center of active sites, J. Am. Chem. Soc. 139 (2017) 1878–1884.

[6] M. Wang, L. Chen, L. Sun, Recent progress in electrochemical hydrogen production with earth-abundant metal complexes as catalysts, Energy Environ. Sci. 5 (2012) 6763–6778.

[7] V.R. Stamenkovic, D. Strmcnik, P.P. Lopes, N.M. Markovic, Energy and fuels from electrochemical interfaces, Nat. Mater. 16 (2016) 57.

[8] Y.-Y. Ma, C.-X. Wu, X.-J. Feng, H.-Q. Tan, L.-K. Yan, Y. Liu, Z.-H. Kang, E.-B. Wang, Y.-G. Li, Highly efficient hydrogen evolution from seawater by a low-cost and stable CoMoP@C electrocatalyst superior to Pt/C, Energy Environ. Sci. 10 (2017) 788–798.

[9] S. Gupta, N. Patel, R. Fernandes, R. Kadrekar, A. Dashora, A.K. Yadav, D. Bhattacharyya, S.N. Jha, A. Miotello, D.C. Kothari, Co–Ni–B nanocatalyst for efficient hydrogen evolution reaction in wide pH range, Appl. Catal. B 192 (2016) 126–133.

[10] Z. Wu, J. Wang, R. Liu, K. Xia, C. Xuan, J. Guo, W. Lei, D. Wang, Facile preparation of carbon sphere supported molybdenum compounds (P, C and S) as hydrogen evolution electrocatalysts in acid and alkaline electrolytes, Nano Energy 32 (2017) 511–519.

[11] Z. Wang, X. Ren, Y. Luo, L. Wang, G. Cui, F. Xie, H. Wang, Y. Xie, X. Sun, An ultrafine platinum–cobalt alloy decorated cobalt nanowire array with superb activity toward alkaline hydrogen evolution, Nanoscale 10 (2018) 12302–12307.

[12] T. Liu, D. Liu, F. Qu, D. Wang, L. Zhang, R. Ge, S. Hao, Y. Ma, G. Du, A.M. Asiri, L. Chen, X. Sun, Enhanced electrocatalysis for energy-efficient hydrogen production over CoP catalyst with Nonelectroactive Zn as a promoter, Adv. Energy Mater. 7 (2017) 1700020.

[13] J. Tian, Q. Liu, A.M. Asiri, X. Sun, Self-Supported Nanoporous Cobalt Phosphide Nanowire Arrays: An Efficient 3D Hydrogen-Evolving Cathode over the Wide Range of pH 0–14, J. Am. Chem. Soc. 136 (2014) 7587–7590.

[14] X. Zou, Y. Zhang, Noble metal-free hydrogen evolution catalysts for water splitting, Chem. Soc. Rev. 44 (2015) 5148–5180.

[15] P.D. Tran, T.V. Tran, M. Orio, S. Torelli, Q.D. Truong, K. Nayuki, Y. Sasaki, S.Y. Chiam, R. Yi, I. Honma, J. Barber, V. Artero, Coordination polymer structure and revisited hydrogen evolution catalytic mechanism for amorphous molybdenum sulfide, Nat. Mater. 15 (2016) 640–646.

[16] H. Zhou, F. Yu, Y. Liu, J. Sun, Z. Zhu, R. He, J. Bao, W.A. Goddard, S. Chen, Z. Ren, Outstanding hydrogen evolution reaction catalyzed by porous nickel diselenide electrocatalysts, Energy Environ. Sci. 10 (2017) 1487–1492.

[17] Z. Pu, S. Wei, Z. Chen, S. Mu, Flexible molybdenum phosphide nanosheet array electrodes for hydrogen evolution reaction in a wide pH range, Appl. Catal. B 196 (2016) 193–198.

[18] H. Jin, X. Liu, Y. Jiao, A. Vasileff, Y. Zheng, S.-Z. Qiao, Constructing tunable dual active sites on two-dimensional C_3N_4@MoN hybrid for electrocatalytic hydrogen evolution, Nano Energy 53 (2018) 690–697.

[19] B. Zhang, J. Liu, J. Wang, Y. Ruan, X. Ji, K. Xu, C. Chen, H. Wan, L. Miao, J. Jiang, Interface engineering: the $Ni(OH)_2$/MoS_2 heterostructure for highly efficient alkaline hydrogen evolution, Nano Energy 37 (2017) 74–80.

[20] Y. Ji, L. Yang, X. Ren, G. Cui, X. Xiong, X. Sun, Nanoporous CoP_3 nanowire array: acid etching preparation and application as a highly active electrocatalyst for the hydrogen evolution reaction in alkaline solution, ACS Sustain. Chem. Eng. 6 (2018) 11186–11189.

[21] C. Tang, L. Gan, R. Zhang, W. Lu, X. Jiang, A.M. Asiri, X. Sun, J. Wang, L. Chen, Ternary $Fe_xCo_{1-x}P$ nanowire array as a robust hydrogen evolution reaction electrocatalyst with Pt-like activity: experimental and theoretical insight, Nano Lett. 16 (2016) 6617–6621.

[22] A. Le Goff, V. Artero, B. Jousselme, P.D. Tran, N. Guillet, R. Métayé, A. Fihri, S. Palacin, M. Fontecave, From hydrogenases to noble metal–Free catalytic nanomaterials for H_2 production and uptake, Science 326 (2009) 1384–1387.

[23] V.S. Thoi, Y. Sun, J.R. Long, C.J. Chang, Complexes of earth-abundant metals for catalytic electrochemical hydrogen generation under aqueous conditions, Chem. Soc. Rev. 42 (2013) 2388–2400.

[24] I. Roger, M.A. Shipman, M.D. Symes, Earth-abundant catalysts for electrochemical and photoelectrochemical water splitting, Int. Rev. Chem. Eng. 1 (2017) 0003.

[25] R. Liu, G. Zhang, H. Cao, S. Zhang, Y. Xie, A. Haider, U. Kortz, B. Chen, N.S. Dalal, Y. Zhao, L. Zhi, C.-X. Wu, L.-K. Yan, Z. Su, B. Keita, Enhanced proton and electron reservoir abilities of polyoxometalate grafted on graphene for high-performance hydrogen evolution, Energy Environ. Sci. 9 (2016) 1012–1023.

[26] W. Cui, Q. Liu, Z. Xing, A.M. Asiri, K.A. Alamry, X. Sun, MoP nanosheets supported on biomass-derived carbon flake: one-step facile preparation and application as a novel high-active electrocatalyst toward hydrogen evolution reaction, Appl. Catal. B 164 (2015) 144–150.

[27] J. Wang, W. Cui, Q. Liu, Z. Xing, A.M. Asiri, X. Sun, Recent progress in cobalt-based heterogeneous catalysts for electrochemical water splitting, Adv. Mater. 28 (2016) 215–230.

[28] H.I. Karunadasa, C.J. Chang, J.R. Long, A molecular molybdenum-oxo catalyst for generating hydrogen from water, Nature 464 (2010) 1329–1333.

[29] N. Joseph, J. Varghese, T. Siponkoski, M. Teirikangas, M.T. Sebastian, H. Jantunen, Glass-free CuMoO4 ceramic with excellent dielectric and thermal properties for ultralow temperature cofired ceramic applications, ACS Sustain. Chem. Eng. 4 (2016) 5632–5639.

[30] J.S. Woertink, P.J. Smeets, M.H. Groothaert, M.A. Vance, B.F. Sels, R.A. Schoonheydt, E.I. Solomon, A $[Cu_2O]^{2+}$ core in Cu-ZSM-5, the active site in the oxidation of methane to methanol, Proc. Natl. Acad. Sci. 106 (2009) 18908–18913.

[31] J. Baltrusaitis, B. Mendoza-Sanchez, V. Fernandez, R. Veenstra, N. Dukstiene, A. Roberts, N. Fairley, Generalized molybdenum oxide surface chemical state XPS determination via informed amorphous sample model, Appl. Surf. Sci. 326 (2015) 151–161.

[32] M.C. Biesinger, Advanced analysis of copper X-ray photoelectron spectra, Surf. Interface Anal. 49 (2017) 1325–1334.

[33] M. Koop, H. Müller-Buschbaum, Zur Kenntnis eines neuen kupfermolybdats: $Cu_4Mo_5O_{17}$, Z. Anorg. Allg. Chem. 530 (1985) 7–15.

[34] A. Moini, R. Peascoe, P.R. Rudolf, A. Clearfield, Hydrothermal synthesis of copper molybdates, Inorg. Chem. 25 (1986) 3782–3785.

[35] E.M. McCarron, J.C. Calabrese, Synthesis and structure of $Cu_4^{1+}Mo_5^{6+}O_{17}$, J. Solid State Chem. 65 (1986) 215–224.

[36] P.D. Tran, M. Nguyen, S.S. Pramana, A. Bhattacharjee, S.Y. Chiam, J. Fize, M.J. Field, V. Artero, L.H. Wong, J. Loo, J. Barber, Copper molybdenum sulfide: a new efficient electrocatalyst for hydrogen production from water, Energy Environ. Sci. 5 (2012) 8912–8916.

[37] B. Beverskog, I. Puigdomenech, Revised pourbaix diagrams for copper at 25 to 300°C, J. Electrochem. Soc. 144 (1997) 3476–3483.

[38] L. Ma, Y. Hu, R. Chen, G. Zhu, T. Chen, H. Lv, Y. Wang, J. Liang, H. Liu, C. Yan, H. Zhu, Z. Tie, Z. Jin, J. Liu, Self-assembled ultrathin NiCo2S4 nanoflakes grown on Ni foam as high-performance flexible electrodes for hydrogen evolution reaction in alkaline solution, Nano Energy 24 (2016) 139–147.

[39] L. Zhang, L. Han, H. Liu, X. Liu, J. Luo, Potential-cycling synthesis of single platinum atoms for efficient hydrogen evolution in neutral media, Angew. Chem. Int. Ed. 56 (2017) 13694–13698.

[40] B. You, X. Liu, G. Hu, S. Gul, J. Yano, D.-e. Jiang, Y. Sun, Universal surface engineering of transition metals for superior electrocatalytic hydrogen evolution in neutral water, J. Am. Chem. Soc. 139 (2017) 12283–12290.

[41] C. Hu, Q. Ma, S.-F. Hung, Z.-N. Chen, D. Ou, B. Ren, H.M. Chen, G. Fu, N. Zheng, In situ electrochemical production of ultrathin nickel nanosheets for hydrogen evolution electrocatalysis, Chem 3 (2017) 122–133.

[42] J.O.M. Bockris, A.K.N. Reddy, Modern Electrochemistry, 2nd ed., Plenum Press, New York, 1998.

[43] D.W. Kirk, A.E. Ledas, Precipitate formation during sea water electrolysis, Int. J. Hydrogen Energy 7 (1982) 925–932.

[44] S.-X. Guo, J. Zhang, D.M. Elton, A.M. Bond, Fourier transform large-amplitude alternating current cyclic voltammetry of surface-bound azurin, Anal. Chem. 76 (2004) 166–177.

[45] J. Zhang, S.-X. Guo, A.M. Bond, Discrimination and evaluation of the effects of uncompensated resistance and slow electrode kinetics from the higher harmonic components of a fourier transformed large-amplitude alternating current voltammogram, Anal. Chem. 79 (2007) 2276–2288.

[46] Y. Liu, S.-X. Guo, A.M. Bond, J. Zhang, Y.V. Geletii, C.L. Hill, Voltammetric determination of the reversible potentials for $[\{Ru_4O_4(OH)_2(H_2O)_4\}(\gamma\text{-}SiW_{10}O_{36})_2]^{10-}$ over the pH range of 2–12: electrolyte dependence and implications for water oxidation catalysis, Inorg. Chem. 52 (2013) 11986–11996.

[47] S.-X. Guo, Y. Liu, C.-Y. Lee, A.M. Bond, J. Zhang, Y.V. Geletii, C.L. Hill, Graphene-supported $[\{Ru_4O_4(OH)_2(H_2O)_4\}(\gamma\text{-}SiW_{10}O_{36})_2]^{10-}$ for highly efficient electrocatalytic water oxidation, Energy Environ. Sci. 6 (2013) 2654–2663.

[48] E.J. Sundstrom, X. Yang, V.S. Thoi, H.I. Karunadasa, C.J. Chang, J.R. Long, M. Head-Gordon, Computational and experimental study of the mechanism of hydrogen generation from water by a molecular molybdenum-oxo electrocatalyst, J. Am. Chem. Soc. 134 (2012) 5233–5242.

[49] Y. Zhang, A.N. Simonov, J. Zhang, A.M. Bond, Fourier transformed alternating current voltammetry in electromaterials research: direct visualisation of important underlying electron transfer processes, Curr. Opin. Electrochem. 10 (2018) 72–81.

[50] S.-X. Guo, A.M. Bond, J. Zhang, Fourier transformed large amplitude alternating current voltammetry: principles and applications, Rev. Polarogr. 61 (2015) 21–32.

[51] A.M. Bond, D. Elton, S.-X. Guo, G.F. Kennedy, E. Mashkina, A.N. Simonov, J. Zhang, An integrated instrumental and theoretical approach to quantitative electrode kinetic studies based on large amplitude Fourier transformed a.c. voltammetry: a mini review, Electrochem. Commun. 57 (2015) 78–83.

[52] D.J. Evans, C.J. Pickett, Chemistry and the hydrogenases, Chem. Soc. Rev. 32 (2003) 268–275.